Monthly Notices
of the
ROYAL ASTRONOMICAL SOCIETY

Mon. Not. R. Astron. Soc. **427,** 2975–2984 (2012) doi:10.1111/j.1365-2966.2012.22018.x

Identifying Type IIn supernova progenitors in our Galaxy: the circumstellar environment of the Galactic luminous blue variable candidate Gal 026.47+0.02

G. Umana,[1⋆] A. Ingallinera,[2] C. Trigilio,[1] C. S. Buemi,[1] P. Leto,[1] C. Agliozzo,[1] A. Noriega-Crespo,[3] N. Flagey,[4] R. Paladini[5] and S. Molinari[6]

[1]*INAF-Osservatorio Astrofisico di Catania, Via S. Sofia 78, 95123 Catania, Italy*
[2]*Dipartimento di Fisica e Astronomia, Università di Catania, Via S. Sofia 64, 95123 Catania, Italy*
[3]*Infrared Processing and Analysis Center, California Institute of Technology, 1200 E. California Blvd, Pasadena, CA 91125, USA*
[4]*Jet Propulsion Laboratory, California Institute of Technology, 4800 Oak Grove Drive, Pasadena, CA 91109, USA*
[5]*NASA Herschel Science Center, California Institute of Technology, 1200 E. California Blvd, Pasadena, CA 91125, USA*
[6]*INAF-Istituto di Astrofisica e Planetologia Spaziali, via Fosso del Cavaliere 100, 00133 Roma, Italy*

Accepted 2012 August 30. Received 2012 August 20; in original form 2012 March 7

ABSTRACT

New data from the *Herschel* Infrared Galactic Plane Survey (Hi-GAL) and the Expanded Very Large Array, together with ancillary multifrequency data from different archives, have provided a comprehensive picture of the circumstellar envelope (CSE) surrounding the Galactic luminous blue variable (LBV) candidate Gal 026.47+0.02. The high angular resolution of both the 70-μm and 6-cm maps has allowed us to appreciate finest details of the nebula, whose morphology is consistent with a series of nested tori. The inner torus, which is close to the central object, is fully ionized, indicating events of aspherical mass loss.

We have derived the physical properties of the CSE, including, in particular, one of the highest current-day mass losses from the central object and a very massive nebula, which consists of, at least, 17 $M_\odot$ of ionized gas, with 1.2–3.2 $\times$ 10^{-2} $M_\odot$ in the form of dust. Altogether, the physical properties of Gal 026.47+0.02, including a very high stellar luminosity, point towards a very massive progenitor on the main sequence.

According to the current models for Type IIn supernovae, the CSEs associated with possible progenitors have well constrained properties in both content and morphology. The derived physical characteristics of the nebula associated with Gal 026.47+0.02 actually satisfy all such requirements, providing some observational evidence of a direct link between a LBV and a possible Type IIn supernova.

Key words: stars: early-type – stars: individual: Gal 026.47+0.02 – stars: winds, outflows – infrared: stars – continuum: stars.

1 INTRODUCTION

Luminous blue variables (LBVs) are massive ($M \sim 22$–$120\,M_\odot$), intrinsically bright ($L \geq 10^{5.8}$ $L_\odot$), evolved objects in a brief ($\sim 10^5$ yr) hot supergiant phase (Vink 2012), in the path leading to Wolf–Rayet (WR) stars, located close to the Humphreys–Davidson limit (Humphreys 2003).

To be defined as a LBV, a star must fulfil a number observational conditions, which include spectroscopic and photometric variabilities with different amplitudes and different time-scales. Such manifestations are usually associated with episodes of enhanced mass loss, with typical rates of the order of 10^{-5}–10^{-4} $M_\odot$ yr^{-1}. In some cases (i.e. η Carinae), giant eruptions can occur with typical optical/near-infrared amplitudes up to 3 mag and with durations of several decades. During a giant eruption, the central star might eject as much as a solar mass or more, with a total energetic output comparable to that of a supernova (SN; Humphreys, Davidson & Smith 1999). The cause of these variabilities is not understood in detail, but it appears to be connected to the proximity to the Eddington limit. In this region on the Hertzsprung–Russell (HR) diagram, the stellar luminosity reaches the Eddington limit ($L_{\rm Edd} \sim L_{\rm star}/M$) and instabilities develop in the stellar atmosphere, leading to strong mass ejections with drastic changes in stellar properties.

Although eruptive events are very rarely witnessed, the presence of visible (Hα) extended circumstellar nebulae around LBVs

⋆E-mail: gumana@oact.inaf.it

suggests that they are a common aspect of LBV behaviour (Nota et al. 1995). Weis (2008) has pointed out that bipolar morphologies are quite often observed in the nebulae associated with LBVs in our Galaxy and in the Magellanic Clouds. However, at present, it is unclear whether this is the effect of a pre-existing density contrast, shaping a more or less isotropic mass-loss event, or whether the wind itself is aspherical (Frank, Ryu & Davidson 1998).

At some distance from the central star, the temperature of the stellar ejecta drops below the condensation temperature of certain mineral compounds, providing the physical conditions for dust to form. Indeed, most of the extended circumstellar envelopes (CSEs) around known LBVs contain huge quantities of dust. Many of these have been detected by *IRAS*, the *Midcourse Space Experiment* (*MSX*) and *Spitzer*, and they have been found to have a mid-infrared and far-infrared excess and a spatially resolved shell (Egan et al. 2002; Clark et al. 2003; Gvaramadze, Kniazev & Fabrika 2010; Umana et al. 2010, 2011a; Wachter et al. 2010). Recently, Kochanek (2011) has pointed out that dust formation in the ejecta of massive stars can occur only during enhanced mass-loss episodes, because the high mass-loss rate ($\dot{M} \geq 10^{-2.5}\,\mathrm{M}_{\odot}\ \mathrm{yr}^{-1}$) provides the non-dust opacity of the wind necessary to self-shield the dust formation region. In this framework, the presence of a dust nebula around a LBV should be taken as circumstantial evidence that an outburst or an enhanced mass-loss episode should have occurred. Such shells provide a baseline to probe the mass-loss history of the central star.

There is observational evidence to indicate that the mass-loss rates of O-type stars are lower than previously thought (Bouret et al. 2005). Together with copious mass-loss episodes associated with the LBV phase, this supports the hypothesis that LBVs might have a key role in the evolution of massive stars, representing the crucial phase during which a star with $M_{\mathrm{MS}} \geq 22\,\mathrm{M}_{\odot}$ has to lose enough mass to become a WR star (Lamers et al. 2001). However, a good test of the current evolutionary models of massive stars requires good knowledge of a key parameter, i.e. the total mass, of both gas and dust lost during the LBV phase, which is actually not well constrained. Moreover, many other questions regarding the LBV phenomenon are still open and deserve attention. For example, during the evolution of a mass-losing star, its mass-loss history will be imprinted in the circumstellar environment. Since several authors have recently suggested that LBVs can be direct progenitors of some core-collapse SNe (van Dyk 2010), it is expected that the structure of LBV ejecta might also influence the geometry of SN remnants and the time light curves (Vink & Kotak 2007; Miller et al. 2010).

Important information on the mass-loss behaviour of the central stars, on quasi-steady versus multiple events and on the origin of the observed morphologies can be gathered by using multiwavelength observations, tracing the different emitting components that coexist in the nebula surrounding the LBVs. Clues about current mass loss can be derived via direct observations of stellar winds (ionized gas component). From the gas and dust distribution, it is possible to evaluate the total mass of the nebula, while the mass-loss history of the central star can be recovered using an analysis of the dusty nebula, pointing out the presence of different shells associated with different periods of mass loss. Finally, from the comparison of maps of different components, it is possible to detect particular features that can be associated with the formation/shaping mechanism. Such an approach has been used, and very interesting results have been achieved so far for several Galactic LBVs (see Umana et al. 2011b for a recent summary).

1.1 Gal 026.47+0.02

The possibility that Gal 026.47+0.02 could be a LBV candidate was put forward by Clark et al. (2003), based on an extended (80 arcsec or 2.5 pc at a distance of 6.5 kpc) dusty nebula detected with the *MSX*, very similar to the nebulae found around the LBV candidates G79.29+0.46 and Wra 17–96 (Egan et al. 2002). Clark et al. (2003) carried out near-infrared spectroscopy of the central star, revealing a rich emission-line spectrum with typical H I, He II, Na, Mg II and low excitation metal features, mostly from [Fe II]. Finally, by applying a non-local thermodynamic equilibrium (NLTE) model to the *K*-band spectrum, the physical parameters of the central star have been obtained: $T = 1.7 \times 10^4$ K, $\log(\mathrm{L/L}_{\odot}) = 6$ and $\dot{M} = 9 \times 10^{-5}\,\mathrm{M}_{\odot}\ \mathrm{yr}^{-1}$. This places Gal 026.47+0.02 very close to the Humphreys–Davidson limit for massive stellar objects.

Some photometric variability has been suggested by Clark et al. (2003). In 2009, Wachter et al. (2010) carried out *K*-band spectroscopic observations, which did not reveal any significant difference from the observations of Clark et al. (2003) obtained between 2001 and 2002. This indicates that Gal 026.47+0.02 does not show any variability, at least on this time-scale, in its spectrum.

In this paper, we present the results of a multiwavelength study of the circumstellar material surrounding the Galactic LBV candidate Gal 026.47+0.02. In the following analysis, we have assumed the distance of 6.5 kpc to Gal 026.47+0.02, as indicated by Clark et al. (2003). However, Clark et al. (2003) have clearly stated that such a distance to Gal 026.47+0.02 is a maximum distance. Throughout the paper, all physical parameters, both stellar and nebular, have been derived with such a caveat in mind, and scaling relations for all the estimated quantities have been provided.

2 DATA/MID-INFRARED

2.1 *Herschel*/Hi-GAL

Images of the position of Gal 026.47+0.02 have been extracted from the *Herschel* Infrared Galactic Plane Survey (Hi-GAL) maps. Hi-GAL (Molinari et al. 2010) is a key project of the *Herschel* satellite, aimed at mapping the inner part of the Galactic plane ($+70^{\circ} \geq l \geq -70^{\circ}$, $|b| \leq 1^{\circ}$), using two photometric bands from the Photoconductor Array Camera and Spectrometer (PACS) and three from the Spectral and Photometric Imaging Receiver (SPIRE). The observations were carried out in parallel mode, using both instruments simultaneously, acquiring images at 70 and 160 μm for PACS, and at 250, 350 and 500 μm for SPIRE. Typical spatial resolutions of these bands are 6.7, 11, 18, 25 and 37 arcsec, respectively. The *Herschel* data were reduced with a specialized reduction pipeline (Traficante et al. 2011) optimized for data affected by a bright and irregular background, which is typical for regions close to or in the Galactic plane.

2.2 *Spitzer*/GLIMPSE and MIPSGAL

The *Spitzer* Galactic Legacy Infrared Mid-Plane Survey Extraordinaire (GLIMPSE; Benjamin et al. 2003; Churchwell et al. 2009) mapped part of the Galactic plane ($+60^{\circ} \geq l \geq -60^{\circ}$, $|b| \leq 1^{\circ}$) with the Infrared Array Camera (IRAC) on board the *Spitzer Space Telescope*. In particular, data for Gal 026.47+0.02 were obtained from the first release (GLIMPSE I). The IRAC has four filters centred at 3.55 μm ($\Delta\lambda = 0.75$ μm), at 4.49 μm ($\Delta\lambda = 1.90$ μm), at 5.73 μm ($\Delta\lambda = 1.42$ μm) and at 7.872 μm ($\Delta\lambda = 2.90$ μm). The

observations were carried out with a spatial resolution of 0.6 arcsec pixel^{-1}, corresponding to an angular resolution that varied between ∼1.7 and ∼2 arcsec.

The Multiband Imaging Photometer for *Spitzer* (MIPS) Galactic Plane Survey (MIPSGAL; Carey et al. 2009) mapped the same region of the Galactic plane as GLIMPSE, using the MIPS in two photometric bands, centred at 24 and 70 μm. Data for Gal 026.47+0.02 were obtained from the third release. In the following analysis, we use only the 24-μm map, characterized by an angular resolution of ∼6 arcsec. Both GLIMPSE and MIPSGAL were retrieved via the online services of the IPAC Infrared Science Archive (IRSA).

2.3 *WISE*

The *Wide-field Infrared Survey Explorer* (*WISE*; Wright et al. 2010) has carried out observations of the entire sky (i.e. the Mid-Infrared All-Sky Survey). This survey provides images at four infrared bands, centred at 3.4, 4.6, 12 and 22 μm, with angular resolutions of 6.1, 6.4, 6.5 and 12.0 arcsec, respectively. For this work, only the *WISE* image at 22 μm has been retrieved from the primary release data products (IRSA).

3 DATA/RADIO

Gal 026.47+0.02 was observed at 5 GHz with the Expanded Very Large Array (EVLA) on 2010 March 14 (project AU129). The observation was carried out in the D configuration, with a bandwidth of 256 MHz, for a total of 10 min on-source time. 3C286 was observed as a flux and bandpass calibrator, while J1822–0938 was observed as a phase calibrator.

A VLA archive search was also performed, retrieving data only for projects where, even if Gal 026.47+0.02 was not the main target, the array was pointed at a position less than 15 arcmin/ν (GHz) away from the phase centre (i.e. within one-third of the primary beam).

Data were found and retrieved at 1.4 GHz (*L* band) in B, C and D configurations (AH707), at 5 GHz (*C* band) in C configuration (AR539), at 8.4 GHz (*X* band) in B configuration (AL647) and at 15 GHz (*U* band) in C configuration (AR539). Details of the archive data set are summarized in Table 1, which also shows the project code, the year when the observations took place, the array configuration, the observing frequency and the corresponding synthetic beam. Both new data and archive data were processed within the Common Astronomical Software Applications (CASA) package, version 3.0.2., following the standard procedures.

The *L* and *C* bands have more than one configuration available. At each frequency, data from each configuration were first independently calibrated and then combined into a single UV data set, providing multiconfiguration maps at 1.4 and 5 GHz. The imaging process was performed by setting the Briggs robust parameter equal to 0. This is a compromise between uniform weighting of the baseline for highest angular resolution and natural weighting for highest sensitivity, and it results in a synthetic beam of 12.2 × 10.8 arcsec^2 and a rms noise of 0.5 mJy beam^{-1} at 1.4 GHz and of 10.5 × 8.9 arcsec^2 and a rms noise of 0.18 mJy beam^{-1} at 5 GHz. Information for the other data set can be found in Table 1. Primary beam correction has been applied for the archive data sets.

The source was also detected at 8.4 GHz (band *X*, configuration B) and 15 GHz (band *U*, configuration C). In both cases, however, because of the high angular resolution, only the central object can be properly mapped.

4 CIRCUMSTELLAR NEBULA

In this section, we illustrate and compare the morphologies observed in different spectral bands as they trace the spatial distribution of different nebular components.

4.1 Dusty component

The central source and the associated nebula have been detected by *Spitzer* (both IRAC and MIPS), by *WISE* and by *Herschel*. The central object is detected in all the IRAC channels (Fig. 1, upper panels), while the presence of a compact, very faint nebula surrounding the central source is, to some extent, evident at 8 μm. In particular, there is a small component, extending for about 15 arcsec and oriented in the south-west direction (labelled with a small 'a' in upper right-hand panel of Fig. 1). The dusty nebula is clearly visible in the *WISE* and MIPS maps (Fig. 1, lower panels). The 24-μm MIPS map has already been presented by Gvaramadze et al. (2010) and Wachter et al. (2010). In the *Herschel* maps, the dusty nebula is detected well only at 70 μm (PACS image), but we cannot exclude the detection in the other *Herschel* channels, because the lower angular resolution and the increasing contribution of the Galactic background at wavelengths ≥70 μm prevent us from clearly isolating the nebula associated with Gal 026.47+0.02.

The morphology of the mid-infrared nebula associated with Gal 026.47+0.02 has already been pointed out by the *MSX* image at ∼21 μm (Clark et al. 2003). It consists of an overall spherical structure, elongated in the north-east and south-west directions, with an average radius of ∼80 arcsec (or ∼2.5 pc at 6.5 kpc), centred on the LBV candidate. The *WISE*, *Spitzer*/MIPS and *Herschel*/PACS maps share a very similar morphology, indicating that they are

Table 1. Summary of radio data including both new EVLA and VLA data archives.

Project	Year	Config.	Band	Beam	Notes
AH707	2001	B	*L*, 20 cm (1.4 GHz)	6.9 × 5.2 arcsec^2	
AH707	2001	C	*L*, 20 cm (1.4 GHz)	22.6 × 18.6 arcsec^2	
AH707	2000	D	*L*, 20 cm (1.4 GHz)	111.6 × 62.4 arcsec^2	
AH707		Multi	*L*, 20 cm (1.4 GHz)	12.2 × 10.8 arcsec^2	*B, C & D concatenation*
AR539	2004	C	*C*, 6 cm (5 GHz)	6.6 × 4.4 arcsec^2	
AU129	2010	D	*C*, 6 cm (5 GHz)	19.9 × 15.5 arcsec^2	*This paper*
AU129/AR539		Multi	*C*, 6 cm (5 GHz)	10.5 × 8.9 arcsec^2	*C & D concatenation*
AL647	2005	B	*X*, 3.6 cm (8.4 GHz)	1.0 × 1.0 arcsec^2	
AR539	2004	C	*U*, 2 cm (15 GHz)	2.2 × 1.5 arcsec^2	

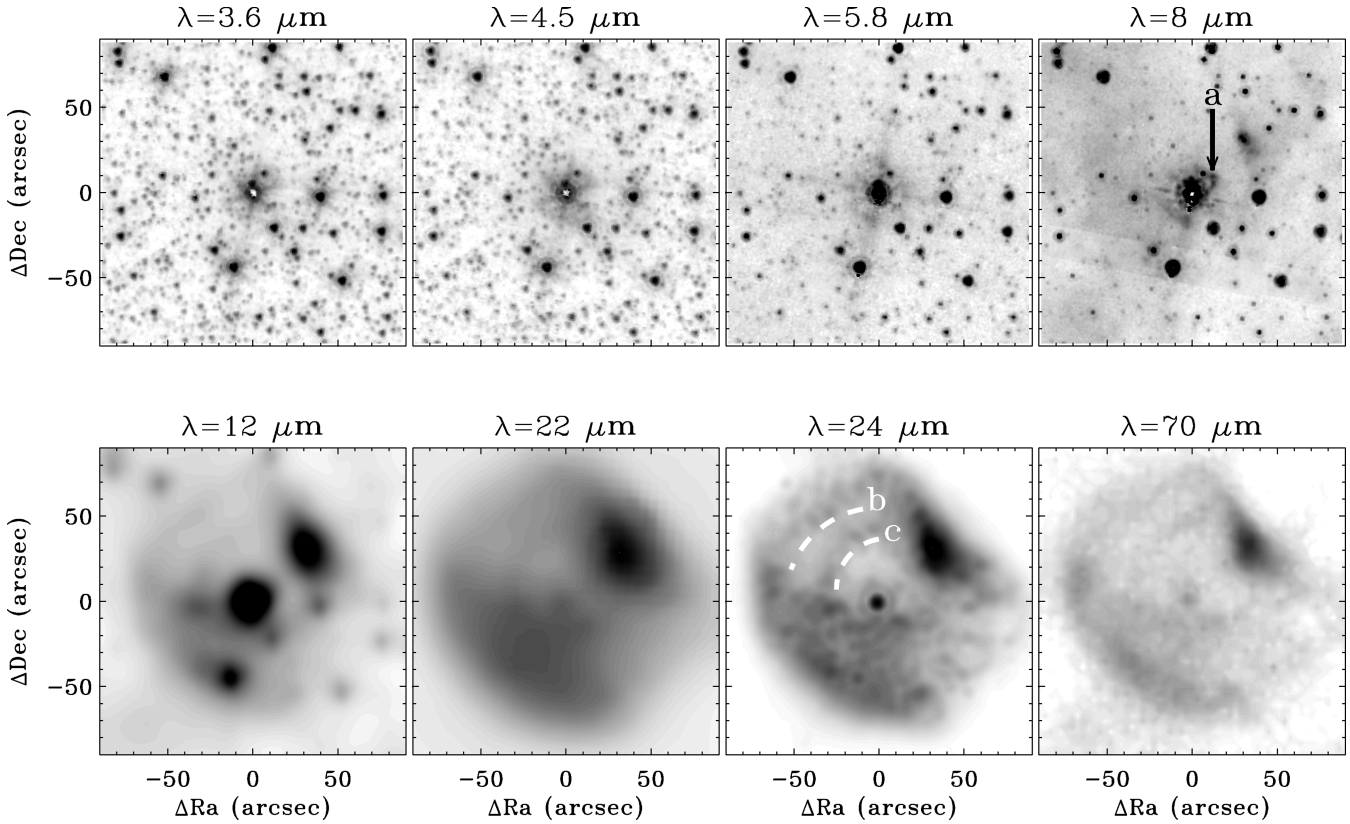

Figure 1. Gal 026.47+0.02 as observed with the IRAC, at 3.6, 4.5, 5.8 and 8 μm (upper panel), with *WISE* at 12 and 22 μm, MIPS at 24 μm and Herschel at 70 μm (lower panel). A small 'a' indicates the structure described in the text, while the small 'b' and 'c' and the corresponding dashed lines highlight the rings observed at 24 and 70 μm.

tracing the same dusty component. However, the 24 *Spitzer* MIPS and 70 μm *Herschel* PACS maps, characterized by a comparable small (∼6 arcsec) angular resolution, point out the finer details of the nebula morphology. They indicate that the dust distribution inside the nebula is not homogeneous, and it has two main regions with higher brightness. The first region, which is more extended, is in the south-east part and the second, which is the brightest, is in the north-west part of the nebula. This bright component is already present in the 8-μm IRAC map. The detailed dust distribution seems to suggest a wrapping of the extended nebula towards the centre. In the 24-μm image, a structure with a partial double ring is also visible in the north-east, with a partial inner ring at ∼30 arcsec and a second partial ring at ∼50 arcsec from the central source. Both rings appear to have an extent of ∼10 arcsec and are also barely visible at 70 μm (labelled with 'b' and 'c' in the third lower panel of Fig. 1).

4.1.1 Temperature and mass of the dust

Aperture photometry has been performed using SKYVIEW,[1] release 3.6, at 24 and 70 μm. In both maps, the flux associated with the source has been evaluated within an area of radius 1.5 arcmin centred on the central source while, for the background, an average value evaluated in an annulus around the nebula has been adopted. We obtain total fluxes of 82.7 ± 2.7 and 94 ± 23 Jy at 24 and 70 μm, respectively.

[1] http://www.ipac.caltech.edu/skyview/

In the hypothesis of an optically thin dusty nebula, where the emission is purely thermal and the dust in the shell is at thermal equilibrium, the observed flux (F_ν) at a given frequency (ν) is given by

$$F_\nu \approx B_\nu(T)\tau_\nu\Omega_S. \quad (1)$$

Here, B_ν and τ_ν are the blackbody expression and the optical depth, respectively, at the given frequency and Ω_S is the solid angle subtended by the source. Therefore, because $\tau_\nu \propto \kappa_\nu$ (the absorption coefficient at the given frequency), from the ratio of the fluxes observed at 24 and 70 μm, assuming a chemical composition and grain size that characterize κ_ν, it is possible to determine the ratio B_{24}/B_{70} and thus the average temperature of the dust $T_{\rm dust}$.

There is growing evidence that dust in Galactic LBVs does not show a simple chemical composition, and both O-rich and C-rich materials have been observed (Egan et al. 2002; Clark et al. 2003; Umana et al. 2010). Following Umana et al. (2010), we compute the absorption coefficient per mass unit for astronomical silicates and graphite for grain sizes of $a = 0.01\,\mu$m using the code CLOUDY (Ferland et al. 1998). This results in $\kappa_{24} = 300$ cm^2 g^{-1} and $\kappa_{70} = 107$ cm^2 g^{-1} for graphite and $\kappa_{24} = 647.7$ cm^2 g^{-1} and $\kappa_{70} = 69$ cm^2 g^{-1} for astronomical silicates. All the following results are derived in both cases, keeping in mind that any combination of O-rich and C-rich materials will provide results between these two extreme cases.

The average dust temperature $T_{\rm dust}$ can be evaluated from B_{24}/B_{70}, obtaining $T_{\rm dust} = 71$ K for astronomical silicates and $T_{\rm dust} = 92$ K for graphite. The average dust temperature, obtained assuming O-rich

dust, is in agreement with results of Clark et al. (2003), which were obtained by assuming a mixture of silicate and Fe grains, where the bulk of the dust mass is in silicate at $T_{\rm dust} \sim 60$ K. Moreover, from equation (1), it is now possible to derive τ_ν, where $\Omega_{\rm S} = 6 \times 10^{-7}$ sr has been evaluated from the maps. We obtain $\tau_{24} \sim 2 \times 10^{-4}$ and $\tau_{70} \sim 2 \times 10^{-5}$ for astronomical silicates and $\tau_{24} \sim 3 \times 10^{-5}$ and $\tau_{70} \sim 10^{-5}$ for graphite, confirming that the dusty nebula is optically thin.

The optical depth can be expressed as

$$\tau_\nu = \kappa_\nu \rho l, \quad (2)$$

where ρl represents the column density. If we integrate the average column density over the source area, given by $\Omega_{\rm S} D^2$, we obtain the total mass of the dust $M_{\rm dust}$, which gives $0.075 \times 10^{-2} D^2_{\rm kpc}\,{\rm M}_\odot$, or $3.2 \times 10^{-2}\,{\rm M}_\odot$, for the assumed distance of 6.5 kpc (Clark et al. 2003), for astronomical silicates and $0.028 \times 10^{-2} D^2_{\rm kpc}\,{\rm M}_\odot$ or $1.2 \times 10^{-2}\,{\rm M}_\odot$ for graphite.

Encouragingly, these values are of the same order of magnitude as the value for $M_{\rm dust}$ (i.e. $0.019\,{\rm M}_\odot$) derived by Clark et al. (2003) on the basis of the modelling of the *MSX* nebula, assuming a dust grain population that consists of a mixture of silicates plus smaller, warm Fe grains.

4.2 Ionized nebula

The 5-GHz image, superimposed on to the 70-μm PACS image, is shown in the left panel of Fig. 2, while a zoom in the radio image (contours) is shown on the right. The presence of a quite interesting radio counterpart to the dusty nebula has already been pointed out by Gvaramadze et al. (2010). The radio nebula consists of a compact component, very probably related to the central star, a more extended (∼40 arcsec), bipolar structure, centred on the compact component and a more diffuse radio emission with a very irregular shape and extending up to ∼100 arcsec. The 1.4-GHz multiconfiguration image, which is is the reprocessed map from the Multiarray Galactic Plane Imaging Survey (MAGPIS; Helfand et al. 2006), essentially reproduced the same morphology as at 5 GHz (see Fig. 3, right panel). At 8.4 GHz, besides the central object, a partially resolved-out nebula is also visible, most notably the bright component in the north-west region. As observed in other Galactic LBVs, such as IRAS 18576+0341 (Umana et al. 2005) and HR Carinae (White 2000), the ionized part of the nebula, traced by the radio emission, is unbalanced, indicating, perhaps, a period of aspherical mass loss from the central object or aspherical ionization of the nebula.

4.2.1 *Current mass loss and total mass of ionized gas*

For the central object, Clark et al. (2003) have derived a mass-loss rate of $\dot{M} = 9 \times 10^{-5}\,{\rm M}_\odot\ {\rm yr}^{-1}$. They derived this mass-loss rate by modelling the infrared spectrum, but with the caveat that they had to adopt a terminal velocity of $v \approx 200$ km s^{-1}, rather than determine it from their modelling, because of the low resolution of their data.

In the case of a stellar wind, no definite boundaries exist. However, it is possible to calculate a representative radius for the emitting source, $R(\nu)$ – where half of the free–free emission at a frequency ν comes from – as function of the physical parameters of the wind (Panagia & Felli 1975). If we assume the physical properties of the wind that have been proposed by Clark et al. (2003), we obtain a representative radius, which, for frequencies $\nu \geq 5$ GHz and for a distance of 6.5 kpc, corresponds to a subarcsec radio source. Such a compact radio source cannot be resolved even with the highest spatial resolution available at the VLA. However, in the higher angular resolution 8.4- and 15-GHz maps, most of the nebula is resolved out and the central component can be clearly distinguished from the background, providing a good determination of its position and flux density.

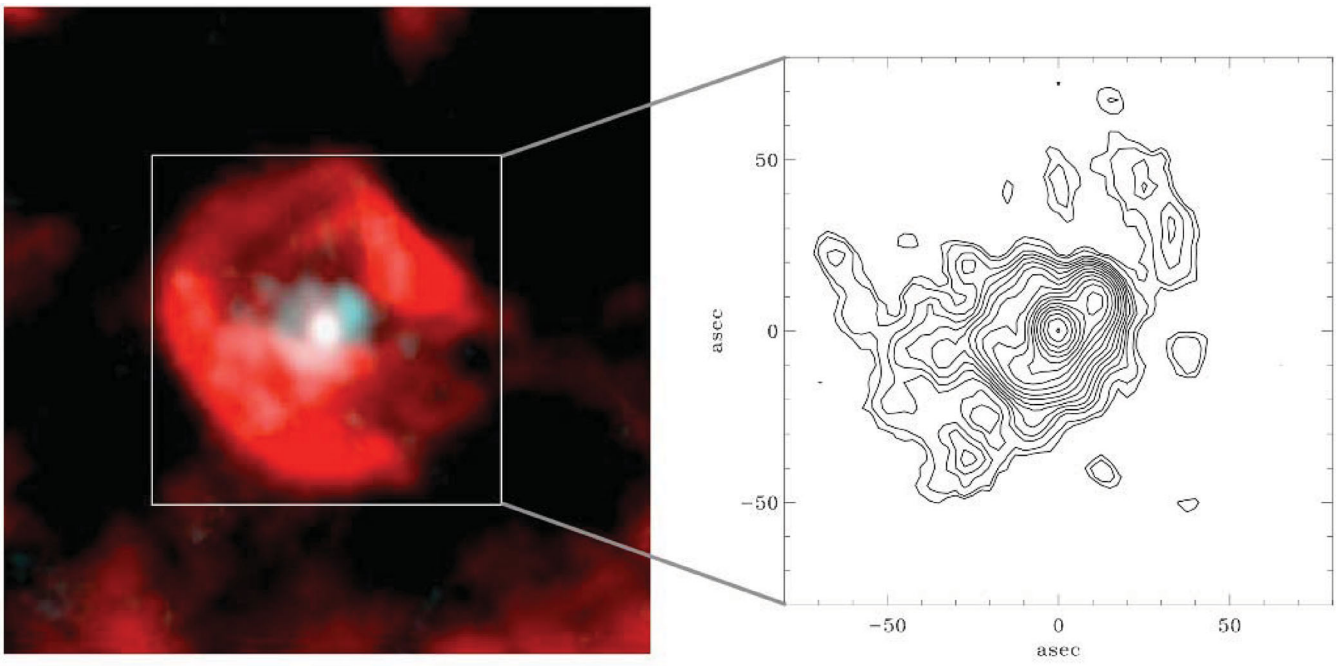

Figure 2. Left: the map of Gal 026.47+0.02 at 5 GHz superimposed on to the 70-μm image (FOV ∼250 arcsec). In the zoom of the radio image (right), the contour levels are $0.18 \times (4, 6, 8, 10, 13, 16, 20, 25, 30, 40, 50, 60, 80, 100, 130, 160, 200)$ mJy beam^{-1}.

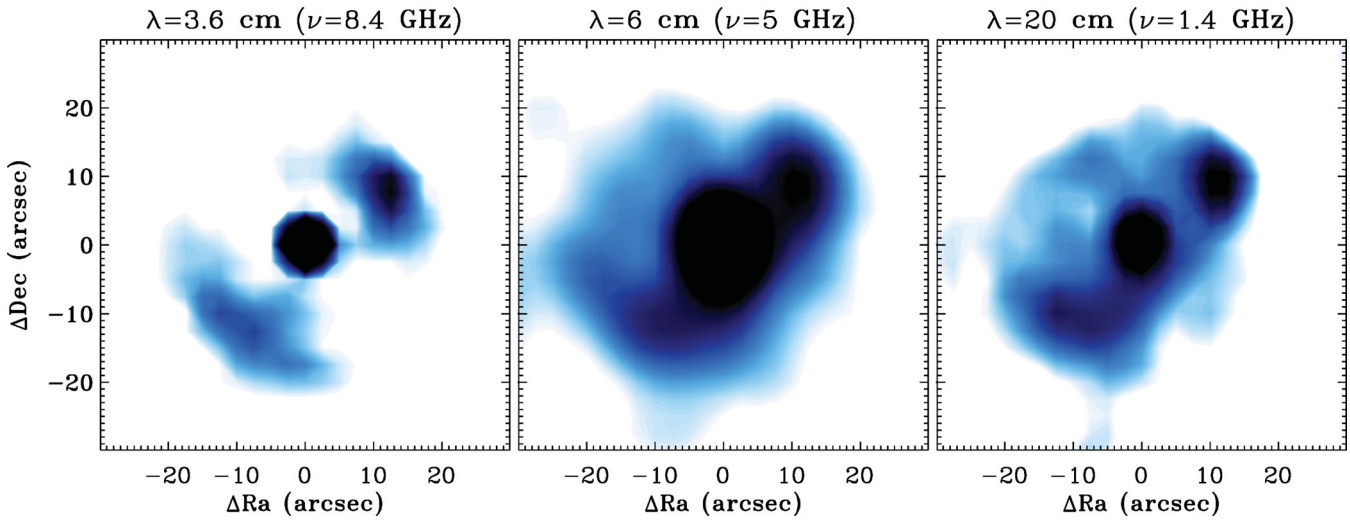

Figure 3. The map of Gal 026.47+0.02 at 8.4 (left), 5 (centre) and 1.4 (right) GHz of the central radio nebula (FOV ∼50 arcsec). The overall structure of the inner nebula is well reproduced in all the images, even if the higher resolution of the 8.4-GHz image prevents the recovery of all the extended emission. The 8.4-GHz image has been convolved with the 1.4-GHz beam. The maps are shown as a percentage of the brightest point in the nebula.

Table 2. Radio flux densities of the central object. Data at 5 GHz are from CORNISH catalogue.

Band (GHz)	Flux density (mJy)
5	35.9 ± 0.4
8.4	43.5 ± 0.14
15	67.1 ± 0.38

The flux density of the central source has been determined using a two-dimensional Gaussian fit (task imfit in CASA). It is 43.5 ± 0.14 and 67.1 ± 0.38 mJy at 8.4 and 15 GHz, respectively, centred at the position $\alpha_{2000} = 18:39:32.24$ and $\delta_{2000} = -05:44:20.17$.

The 5-GHz flux density of the central source of Gal 026.47+0.02 is also reported in the Co-Ordinated Radio 'N' Infrared Survey for High-mass star formation (CORNISH) catalogue (Purcell et al., submitted). The CORNISH is a radio survey of the Galactic plane conducted at 5 GHz with the VLA using B and BnA configurations, with a typical angular resolution of ∼1 arcsec and a rms noise level of 0.4 mJy beam^{-1} (Hoare et al. 2012). The results are summarized in Table 2, indicating a spectral index of $\alpha = 0.68 \pm 0.2$, which is consistent with a stellar wind.

The current-day mass loss from the central star can be estimated by using the standard formulae (Panagia & Felli 1975), relating the radio flux (F_ν, mJy), observed at the frequency ν (Hz), to the dynamical parameters of the wind, i.e. the mass-loss rate; ($\dot{M}$, $M_\odot$ yr^{-1}) and the terminal velocity of the wind (v_∞; km s^{-1}), and assuming full ionization and cosmic abundances:

$$\dot{M} = 6.7 \times 10^{-4} v_\infty F_\nu^{3/4} D_{\rm kpc}^{3/2} (\nu \times g_{\rm ff})^{-0.5} \quad M_\odot\ {\rm yr}^{-1}. \qquad (3)$$

The free–free Gaunt factor ($g_{\rm ff}$) is approximated with $g_{\rm ff} = 9.77[1 + 0.13 \log(T^{3/2}/\nu)]$ (Leitherer & Robert 1991), where T is expressed in K and $D_{\rm kpc}$ is the distance to the source in kpc.

From the radio flux density measured at 5 GHz (Table 2), assuming that the temperature of the plasma of the wind is 10^4 K and assuming a value of $v \approx 200$ km s^{-1} for the stellar velocity, we derive a mass-loss rate of $\dot{M} = 0.11 \times 10^{-4} D_{\rm kpc}^{3/2}\ M_\odot$ yr^{-1}, or $\dot{M} = 1.9 \times 10^{-4}\ M_\odot$ yr^{-1} for the assumed distance of 6.5 kpc (Clark et al. 2003). This value is in a good agreement with that derived by Clark et al. (2003), confirming that Gal 026.47+0.02 has one of the highest current-day mass-loss rates of any known Galactic LBV. We have to stress here that the mass-loss rate also depends on the assumed wind velocity. However, the assumed value for the wind velocity is within the range observed for LBVs and LBV candidates (i.e. 100–250 km s^{-1}; Vink 2012), and we expect this to translate to a factor of 0.5–1.25 in the mass-loss rate.

In the multiconfiguration maps, both compact and extended emissions are correctly mapped, without any loss of brightness, because the extended sources have angular scales (≈100 arcsec), smaller than the fringe spacing corresponding to the shortest baselines of the array (≈900 and ≈300 arcsec at 1.4 and 5 GHz, respectively). The radio flux density of the extended components at 1.4 and 5 GHz have been determined within CASA (casaviewer) by encompassing the emitting region with a polygon region. To accomplish this, at both frequencies, the contribution of the flux resulting from the stellar wind has been subtracted, where, at 1.4 GHz, the value extrapolated from 5 GHz, assuming 0.68 as the spectral index, has been adopted. This results in 110 ± 9.5 and 145 ± 2.16 mJy at 1.4 and 5 GHz, respectively, if the inner 40-arcsec structure is considered only. The flux density of the entire emitting region can be evaluated only at 5 GHz, characterized by a better signal-to-noise ratio, resulting in 220 ± 4.45 mJy. The errors associated with the flux determinations have been calculated as $(N_{\rm beams})^{0.5} \times 3\sigma$, following Brogan et al. (2006), where $N_{\rm beams}$ is the number of independent beams in the considered area and σ is the rms noise level in the maps, evaluated by selecting an empty region of the image.

For the inner 40-arcsec nebula, a spectral index α ($S_\nu \propto \nu^\alpha$) can be estimated. We derive a flat spectral index $\alpha = 0.11 \pm 0.08$, still consistent with optical thin emission.

In the hypothesis of an optically thin nebula, the radio flux density can be used to evaluate the total ionized mass. However, because of the irregular shape of the radio nebula, the application of the standard analytical formulae, which assume a defined geometry (Buckley & Schneider 1995), can in principle lead to wrong estimations of the total ionized mass.

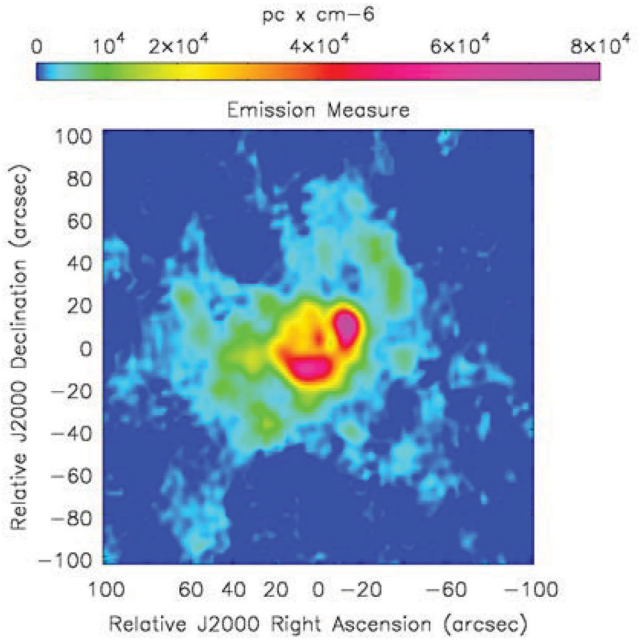

Figure 4. Emission measure map of the nebula around Gal 026.47+0.02. The central radio source associated with the current-day mass loss from the central star has been subtracted.

From the radio map at 5 GHz, after subtracting the central component, which is assumed to have a Gaussian morphology, an optical depth map has be constructed, from $B_{5\mathrm{GHz}} = B(T) \times \tau$ (optically thin hypothesis), where $B_{5\mathrm{GHz}}$ is the source brightness at 5 GHz and $B(T)$ is the blackbody emission evaluated at 5 GHz, adopting a temperature of $T = 10^4$ K for the nebula. From the optical depth map, it is possible to obtain an emission measure map from the expression of τ for free–free emission:

$$\tau = 8.24 \times 10^{-2} T^{-1.35} \left(\frac{\nu}{5\,\mathrm{GHz}}\right)^{-2.1} EM. \quad (4)$$

Here, $EM = \int n_\mathrm{e}^2\,\mathrm{d}l$ indicates the emission measure in cm^{-6} pc. The resulting emission measure map is shown in Fig. 4.

From the emission measure map, after an integration over an area corresponding to the inner nebula, we obtain an average $\langle EM\rangle \approx 30\,000$ cm^{-6} pc.

Assuming that the geometrical depth of the inner component l is equal to the transversal size of the nebula, which subtends an angle of 38 arcsec (1.2 pc at $D = 6.5$ kpc), an average electron density of $\langle n_\mathrm{e}\rangle \approx 160$ cm^{-3} can be estimated, which corresponds to a total mass of ionized gas given by

$$M_\mathrm{ion} = A_\mathrm{source} l \langle n_\mathrm{e}\rangle m_\mathrm{p}/M_\odot. \quad (5)$$

Here, A_source is the area of the source as seen from Earth in cm^2, m_p is the proton mass and l is expressed in cm. This corresponds to a total ionized mass of 7.6 M$_\odot$, for a total area covered by the inner nebula of $A_\mathrm{source} = 1.7$ pc^2.

If we repeat the same calculation, this time for the more extended, lower brightness component of the radio nebula, with depth $l = 2.2$ pc, we obtain $\langle EM\rangle \approx 4500$ cm^{-6} pc and $\langle n_\mathrm{e}\rangle \approx 45$ cm^{-3}, and we derive a total ionized mass of 9.7 M$_\odot$, in a total area of $A_\mathrm{source} = 7.7$ pc^2.

It is remarkable that we find the same order of magnitude of ionized mass in the two radio nebula. If we assume that they are related to different mass-loss episodes, we can conclude that mass loss occurs episodically, but providing almost the same quantity of material each time. However, the obtained value for the total ionized mass in the nebulae is a function of the assumed value of the distance to the source and it will scale as $M_\mathrm{ion} \sim 0.070\, D_\mathrm{kpc}^{5/2}$ M$_\odot$ and $M_\mathrm{ion} \sim 0.035\, D_\mathrm{kpc}^{5/2}$ M$_\odot$ for the inner nebula and the outermost nebula, respectively.

4.3 Comparison of dust and ionized gas

The data analysed in this work, and in particular the 70-μm *Herschel* map and the VLA map, allow a detailed comparison of the dust and ionized gas components. The morphology of both components reveals a very interesting structure, consistent with one or more nested tori, whose common axis is at position angle PA $\sim 315^\circ$. The inner torus is close to the central object and its material is ionized and visible via its radio free–free emission. Such a radio nebula is well confined inside the dusty part of the stellar ejecta. The outermost torus of material is far from the star, where conditions are favourable for dust to condense, and it is visible via thermal dust emission. In between these two main structures, there is also diffuse radio emission, which is extending towards the south-east and north-west parts of the nebula. In particular, a low brightness component appears to be the radio counterpart of the most luminous dusty structure visible from 12 to 70 μm.

The overall structure of the nebula surrounding Gal 026.47+0.02 is very similar to that observed around another LBV candidate, HDE 316285 (Morris et al. 2008). For this source, Hillier et al. (1998) have also reported the presence of a stellar wind with extreme proprieties.

The small structure, observed in the IRAC 8-μm map at PA = 45°, extending up to ∼15 arcsec, appears to be spatially related to the brighter radio component of the inner, ionized torus. To further increase the angular resolution of the IRAC 8-μm map, the basic calibrated data (BCDs) have been reprocessed with the HiREs deconvolution software, A *WISE* Astronomical Image Co-Adder (AWAIC), developed by Masci & Fowler (2009) for the creation of their Atlas images.[2] The AWAIC software optimizes the co-addition of individual frames by making use of the point response function (PRF) as an interpolation kernel, to avoid flux losses in undersampled arrays, such as those of IRAC. It also allows a resolution enhancement (HiRes) of the final image, by removing its effect from the data in the deconvolution process. A similar method has been applied, quite successfully, to the *Spitzer* data of young stellar outflows such as HH 46/47 (Noriega-Crespo et al. 2004a; Velusamy, Langer & Marsh 2007), Cep E (Moro-Martín et al. 2001; Noriega-Crespo et al. 2004b; Velusamy et al. 2011) and HH 1/2 (Noriega-Crespo & Raga 2012). On the IRAC images, the HiRes processing enhances the angular resolution from the standard ∼2 arcsec to ∼0.6–0.8 arcsec (Velusamy et al. 2007; Noriega-Crespo & Raga 2012). In Fig. 5, the radio emission at 8.4 GHz (contours) has been superimposed on to the improved IRAC 8-μm map and a similar morphology is evident. This could indicate that, at 8 μm, we are not seeing a warm dust or polycyclic aromatic hydrocarbon (PAH) contribution, but we are tracing the free–free emission.

The maximum distance at which the ionizing radiation can penetrate a medium of density n_e is given by

$$R_\mathrm{S} = \left(\frac{3\,N_\mathrm{UV}}{4\pi n_\mathrm{e}^2 \beta}\right)^{1/3}, \quad (6)$$

[2] http://wise2.ipac.caltech.edu/staff/fmasci/awaicpub.html

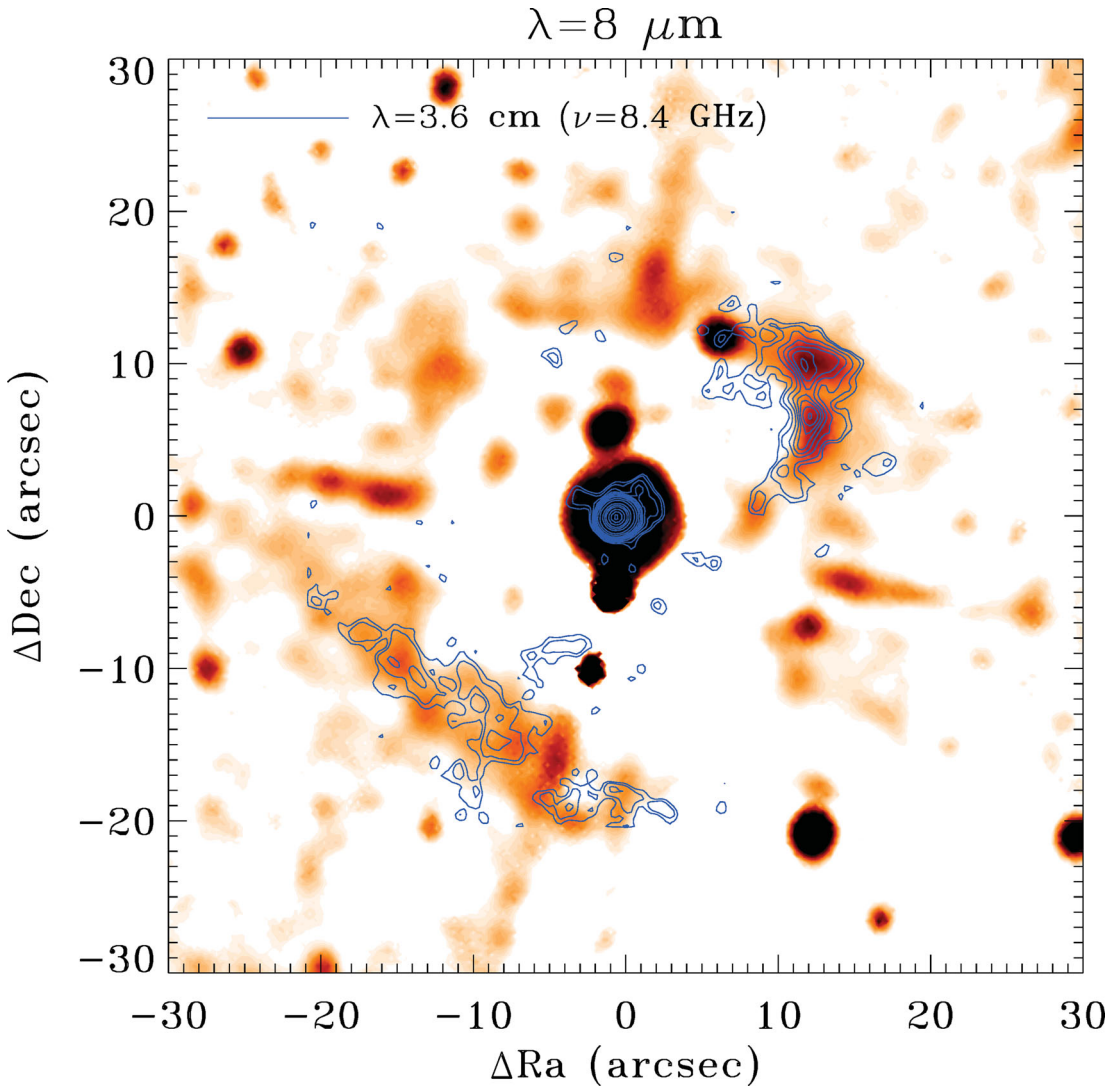

Figure 5. The radio (8.4-GHz) image of Gal 026.47+0.02 superimposed on to the IRAC 8-μm improved image (see text). Even if the high angular resolution partially resolves out the inner radio nebula, the compact (∼10 arcsec) north-west component agrees well with the component seen at 8 μm. The level curves of the 8.4-GHz map are 3, 4, 6, 8, 10, 12, 15, 20, 30, 50, 100, 150, 200, 300, 400 and 500 times the noise of the map. A logarithmic scaling of the levels from the background sky levels to about 25 per cent of the maximum level of the map has been adopted for the 8-μm map to better emphasize the faint structures.

where R_S is expressed in cm, N_{UV} is the number of ionizing photons (photons s^{-1}) emitted by that at the central object and β is the recombination coefficient for H (i.e. $T_e \sim 10^4$ K can be approximated by $\sim 3 \times 10^{-13}$ cm^3 s^{-1}). In equation (6), the same number density for electrons and for neutrons has been assumed ($n_e \sim n_p$). Thus, R_S will scale as $\propto N_{UV}^{1/3}/n_e^{2/3}$.

The average radius of the inner radio nebula is $R_{radio} \sim 19$ arcsec (or ∼0.6 pc). To ionize this region, characterized by n_e, as derived by our radio observations, an ionizing UV radiation flux of $2 \times 10^{47}\, n_{photons}$ s^{-1} is necessary, which corresponds to the radiation field of a B0.5–B1 supergiant, with T_{eff} between 23 600 and 20 400 K (Panagia 1973). According to this, the central object has to be hotter than is consistent with the spectral classification given by Clark et al. (2003). However, this result has been obtained with the caveat that the supergiants considered by Panagia (1973) are less luminous than Gal 026.47+0.02, and this must be taken into account when determining the temperature of the ionizing source. Moreover, the presence of low-excitation features, such as Fe II, Mg II and Na I, seem to indicate that the central object has a lower temperature than that inferred on the basis of the number of ionizing photons required to excite the nebula.

However, there are some other factors that support the fact that there is a more powerful ionizing source associated with the Gal 026.47+0.02 nebula. (i) There is more radio emission behind the compact torus, as indicated by the outermost radio nebula, and still more intense UV radiation is necessary to justify it. (ii) There is a significant quantity of dust in the nebula, competing with the gas in absorbing the UV photons.

By definition, a LBV or a LBV candidate is variable. Even if there is no firm evidence that Gal 026.47+0.02 is variable, in principle, we can assume that Gal 026.47+0.02 has gone though a hotter phase, during which the outermost nebula has been ionized. An ionized nebula with an average density $\langle n_e \rangle$ and a temperature of $T_e \sim 10^4$ K will recombine within $(1.2 \times 10^5)/\langle n_e \rangle$ yr. If we assume that the outermost nebula has an average density of $\langle n_e \rangle \approx 45$ cm^{-3}, as previously derived in Section 4.2, this implies a recombination time of the order of 2600 yr, of the same order of magnitude as the dynamical age of the nebula of (i.e. ∼4000 yr) derived by Clark

et al. (2003). In this framework, the presence of an outermost ionized nebula is also consistent with a previous hotter phase of the central object.

5 CONCLUSION

We have presented new far-infrared data, from the *Herschel* Hi-GAL survey, and new radio data, obtained with the EVLA, of the Galactic LBV candidate Gal 026.47+0.02, with the aim of deriving the morphological and physical characteristics of the associated CSE. To complete the data set and to obtain a picture of the CSE that is as comprehensive as possible, data from mid-infrared surveys, as well as radio data, have been retrieved from several archives.

The high angular resolution of both mid-infrared data (MIPSGAL and Hi-GAL) and radio data (EVLA) has allowed us to study the CSE morphology in detail. This has revealed a very interesting structure, consisting of a series of nested tori around a common axis at position angle PA $\sim 315^\circ$. The inner part of the structure is completely ionized and visible via free–free emission, while the outermost part is traced by thermal emission from dust. We have interpreted this as observational evidence that mass loss occurred not steadily but in different episodes, because the tori appear nested, and it is aspherical.

The central source has a massive current-day mass loss ($1.9 \times 10^{-4}\,M_\odot\,yr^{-1}$) and has to be hotter than has been foreseen by previous tentative spectral classification (Clark et al. 2003). Otherwise, it would not have the UV field necessary to ionize even the inner radio nebula in a dusty environment. However, the previous estimate of $T_{\rm eff}$, as derived by Clark et al. (2003), is still consistent with the observed extended radio emission if we assume the existence of a previous, hotter phase of Gal 026.47+0.02.

From our study, we find that Gal 026.47+0.02 is a remarkable object among Galactic LBV and LBV candidates. It shows one of the higher current-day mass losses and has a very massive CSE, containing, at least, $17\,M_\odot$ just in the ionized part of its extended nebula. Therefore, this has to be considered as a lower limit of the true content in mass of the entire nebula. A number of known Galactic LBVs and LBV candidates appear to have a massive nebula (e.g. Clark et al. 2003), but very few of them have a comparable massive ejecta. We want to note here that the shell mass has been derived directly from the radio, which traces only the ionized gas, but it does not suffer of any effects of dust intrinsic extinction. This is different from other LBVs and LBV candidates where the shell mass has been derived from Hα (Nota et al. 1995), which is strongly affected by absorption, particularly for objects enshrouded by dust, or by extrapolating from the mass of the dust component, assuming a gas-to-dust typical for the interstellar medium.

We find that 3.2×10^{-2} or $1.2 \times 10^{-2}\,M_\odot$ is the dust content of the ejecta, depending on the assumed chemical composition of the dust, and that this dust has an average temperature between $\sim$70 and $\sim$90 K. There is no evidence for warmer dust or PAH contribution, because the only structure of the CSE visible in one of the IRAC channels has a radio counterpart and is therefore related to the ionized gas.

There is growing evidence for a close connection between core-collapse SNs (CCSNs) and LBVs. Several authors have reported observations that point out SN explosions that have occurred in stars in the LBV phase as well as immediately after the LBV phase (Chevalier 2007; Pastorello et al. 2007). There is a peculiar type of CCSN (i.e. Type IIn) that is characterized by optical spectra, indicating strong interaction with the circumstellar environment. These constitute a small fraction of CCSNs, about $\sim$6–9 per cent (Smith et al. 2011a), but they are extremely luminous. In all cases, the extraordinary luminosity of SNe IIn can be modelled as a strong interaction of the SNe shock with the circumstellar environment, whose characteristic in mass, and thus in mass-loss rate, can be ascribed to enhanced mass-loss episodes, as observed in the LBV phase. Moreover, the results from a warm *Spitzer*/IRAC survey of a sample of known SNe IIn indicate that, when mid-infrared emission is detected, it is very likely to be related to a pre-existing dust shell, whose mass content is consistent with LBV progenitors (Fox et al. 2011).

SN 2010jl was a very bright SNe IIn, showing a significant infrared excess, which could be modelled in some detail. In particular, Andrews et al. (2011) modelled the infrared spectral energy distribution of SN 2010jl, which was observed 90 d after the explosion, as consistent with an infrared echo of pre-existing dust, located around SN 2010jl, which was heated by the initial SN flash. They derived the physical parameters of the CSE of the progenitor, which resulted in a torus-like configuration, with a dust mass between 0.03 and $0.35\,M_\odot$, depending on the chemical composition of the dust (amorphous carbon versus silicates) and on the inclination of the dusty torus with respect to the plane of the sky. Assuming a gas-to-dust ratio of 100, this translates into a total mass of the CSE between 3 and $35\,M_\odot$.

The extreme characteristic of the CSE associated with Gal 026.47+0.02 and, in particular, its peculiar aspherical morphology, as derived from the present work, fit quite well with the requirement for the SN 2010jl progenitor, according to the model of Andrews et al. (2011). This may indicate that Gal 026.47+0.02 is a precursor of a Galactic, very bright Type IIn SN, which will explode with the same characteristics as SN 2010jl.

ACKNOWLEDGMENTS

We wish to thank an anonymous referee for suggestions that have helped to improve the paper. This publication makes use of data products from *WISE*, which is a joint project of the University of California, Los Angeles, and the Jet Propulsion Laboratory/California Institute of Technology, funded by the National Aeronautics and Space Administration. The Very Large Array of the National Radio Astronomy Observatory is a facility of the National Science Foundation, operated under cooperative agreement by Associated Universities, Inc. This research is supported by ASI contract I/038/08/0 'HI-GAL'.

REFERENCES

Andrews J. E. et al., 2011, AJ, 142, 45
Benjamin R. A. et al., 2003, PASP, 115, 953
Bouret et al., 2005, A&A, 438, 301
Brogan C. L., Gelfand J. D., Gaensler B. M., Kassim N. E., Lazio T. J. W., 2006, ApJ, 639, 25
Buckley D., Schneider S. E., 1995, ApJ, 446, 279
Carey S. J. et al., 2009, PASP, 121, 76
Chevalier R. A., 2007, in Immler S., Weiler K., eds, AIP Conf. Proc. Vol. 937, Supernova 1987A: 20 Years After: Supernovae and Gamma-Ray Bursters. Am. Inst. Phys., New York, p. 206
Churchwell E. et al., 2009, PASP, 121, 213
Clark J. S., Egan M. P., Crowther P. A., Mizuno D. R., Larionov V. M., Arkharov A., 2003, A&A, 412, 185
Egan M. P., Clark J. S., Mizuno D. R., Carey S. J., Steele I. A., Price S. D., 2002, ApJ, 572, 288
Ferland G. J., Korista K., Vernet D., Ferguson J., Kingdon J., Verner E., 1998, PASP, 110, 761

Fox O. D. et al., 2011, ApJ, 741, 7
Frank A., Ryu D., Davidson K., 1998, ApJ, 500, 291
Gvaramadze V. V., Kniazev A. Y., Fabrika S., 2010, MNRAS, 405, 1047
Helfand D. J. et al., 2006, AJ, 131, 2525
Hillier D. J., Crowther P. A., Najarro F., Fullerton A. W., 1998, A&A, 340, 483
Hoare M. G. et al., 2012, PASP, 124, 939
Humphreys R. M., 2003, in van der Hucht K., Herrero A., Esteban C., eds, Proc. IAU Symp. 212, A Massive Star Odyssey: From Main Sequence to Supernova. Astron. Soc. Pac., San Francisco, p. 38
Humphreys R. M., Davidson K., Smith N., 1999, PASP, 111, 1124
Kochanek C. S., 2011, ApJ, 743, 73
Lamers H. J. et al., 2001, ApJ, 551, 764
Leitherer C., Robert C., 1991, ApJ, 377, 629
Masci F., Fowler J. W., 2009, in Bohlender D. A., Durand D., Dowler P., eds, ASP Conf. Ser. Vol. 411, Astronomical Data Analysis Software and Systems XVIII. Astron. Soc. Pac., San Francisco, p. 67
Miller A. A. et al., 2010, MNRAS, 404, 305
Molinari S. et al., 2010, PASP, 122, 314
Moro-Martín A. et al., 2001, ApJ, 555, 146
Morris P., *Spitzer* WRRINGS team, 2008, in Bresolin F., Crowther P. A., Puls J., eds, Proc. IAU Symp. 250, Massive Stars as Cosmic Engines. Kluwer, Dordrecht, p. 361
Noriega-Crespo A., Raga A. C., 2012, ApJ, 750, 101
Noriega-Crespo A. et al., 2004a, ApJS, 154, 352
Noriega-Crespo A., Moro-Martín A., Carey S., Morris P. W., Padgett D. L., Latter W. B., Muzerolle J., 2004b, ApJS, 154, 402
Nota A., Livio M., Clampin M., Schulte-Ladbeck R., 1995, ApJ, 448, 788
Panagia N., 1973, AJ, 78, 929
Panagia N., Felli M., 1975, A&A, 39, 1
Pastorello A. et al., 2007, Nat, 447, 829
Smith N. et al., 2011a, ApJ, 732, 63
Traficante A. et al., 2011, MNRAS, 416, 2932
Umana G., Buemi C. S., Trigilio C., Leto P., 2005, A&A, 437, L1
Umana G., Buemi C. S., Trigilio C., Leto P., Hora J. L., 2010, ApJ, 717, 1
Umana G., Buemi C. S., Trigilio C., Leto P., Agliozzo C., Ingallinera A., Noriega-Crespo A., Hora J. L., 2011a, ApJ, 739, L11
Umana G., Buemi C. S., Trigilio C., Leto P., Hora J. L., Fazio G., 2011b, Bull. Soc. R. Sci. Liege, 80, 335
van Dyk S. D., 2010, in Lietherer C., Bennett P., Morris P., van Loon J., eds, ASP Conf. Ser. Vol. 425, Hot and Cool: Bridging Gaps in Massive Star Evolution. Astron. Soc. Pac., San Francisco, p. 73
Velusamy T., Langer W. D., Marsh K. A., 2007, ApJ, 668, L159
Velusamy T., Langer W. D., Kumar M. S. N., Grave J. M. C., 2011, ApJ, 741, 60
Vink J. S., 2012, in Davidson K., Humphreys R. M., eds, ASSL Vol. 384, Eta Carinae and the Supernova Impostors. Springer, Berlin, p. 221
Vink J. S., Kotak R., 2007, Rev. Mex. Astron. Astrofis., 30, 17
Wachter S., Mauerhan J. C., Van Dyk S. D., Hoard D. W., Kafka S., Morris P. W., 2010, AJ, 139, 2330
Weis K., 2008, in Hamann W.-R., Feldmeier A., Oskinova L. M., eds, Clumping in Hot-Stars Winds. Universitätsverlag Potsdam, Potsdam, p. 183
White S. M., 2000, ApJ, 539, 851
Wright E. L. et al., 2010, AJ, 140, 1868

This paper has been typeset from a TEX/LATEX file prepared by the author.